# An Interconnected Observer for Concurrent Estimation of Bulk and Surface Concentration in the Cathode and Anode of a Lithium-ion Battery

Anirudh Allam, *Student Member, IEEE*, and Simona Onori, *Senior Member, IEEE*

***Abstract*—Electrochemical state estimation of a lithium-ion battery provides crucial information to the battery management system about its state of charge and state of health. Insight into nonmeasurable electrochemical states, such as bulk and surface concentration, holds the key to improving safety, predicting degradation, and facilitating a wider range of battery operation. Although strategies to estimate concentration in a single electrode are well-researched, the topic of simultaneous concentration estimation in both electrodes is not fully investigated. Real-time knowledge of lithium concentration in both electrodes will be essential in setting operational limits specific to the electrode chemistry, enabling estimation of available power in each electrode, and developing algorithms to monitor or minimize degradation mechanisms occurring at either electrode. To that end, an interconnected sliding mode observer is proposed for the concurrent estimation of bulk and surface concentration in the cathode and anode. An experimentally validated enhanced single particle model forms the basis for the electrochemical-model-based observer design. The novel bidirectional structure of the interconnected observer circumvents the issue associated with the combined concentration estimation in both electrodes. The convergence of the interconnected observer's error dynamics is proved using Lyapunov's stability theory and its performance is verified under measurement noise and parametric uncertainties.**

***Index Terms*—Bulk concentration, interconnected observer, Lithium-ion battery, Lyapunov stability, single particle model, sliding mode observer, surface concentration.**

## NOMENCLATURE

| | |
|---|---|
| $A$ | Cell cross-sectional area [$m^2$]. |
| BMS | Battery management system. |
| $D_e$ | Electrolyte phase diffusion [$m^2$/s]. |
| $D_e^{\text{eff}}$ | Effective electrolyte phase diffusion [$m^2$/s]. |
| $D_{s,j}$ | Solid phase diffusion [$m^2$/s]. |
| $\mathcal{D}_{s,j,\text{ref}}$ | Reference solid phase diffusion [$m^2$/s]. |
| $E_a$ | Activation energy. |
| ESPM | Enhanced single particle model. |
| $EV$ | Electric vehicle. |
| $F$ | Faraday's constant [C/mol]. |
| FDM | Finite-difference method. |
| $G$ | Observer gain. |
| HPPC | Hybrid pulse power characterization. |
| $I_{\text{batt}}$ | Applied current [A]. |
| $L_j$ | Domain thickness [m]. |
| $M$ | Number of cartesian discretization grids. |
| $N$ | Number of radial discretization grids. |
| NMC | Nickel manganese cobalt oxide. |
| ODE | Ordinary differential equation. |
| OCP | Open-circuit potential. |
| PDE | Partial differential equation. |
| $Q_{\text{nom}}$ | Nominal battery capacity. |
| $R_g$ | Universal gas constant [J/mol-K]. |
| $R_j$ | Particle radius [m]. |
| $R_l$ | Lumped resistance [$\Omega$]. |
| RMS | Root mean squared. |
| RUL | Remaining useful life. |
| SEI | Solid electrolyte interphase. |
| SMO | Sliding mode observer. |
| SOC | State of charge. |
| SOH | State of health. |
| SPM | Single particle model. |
| $T$ | Cell temperature [°C]. |
| $T_{\text{ref}}$ | Reference temperature [°C]. |
| $U_j$ | Open-circuit potential [V]. |
| UDDS | Urban dynamometer driving schedule. |
| $V$ | Cell terminal voltage [V]. |
| $a_{s,j}$ | Specific interfacial surface area [$m^{-1}$]. |
| $c_e$ | Concentration in liquid phase [mol/$m^3$]. |
| $c_{e,0}$ | Average liquid phase concentration [mol/$m^3$]. |
| $c_{s,j}$ | Concentration in solid phase [mol/$m^3$]. |
| $c_{s,j,\text{bulk}}$ | Bulk concentration [mol/$m^3$]. |
| $c_{s,j,\text{surf}}$ | Concentration at the surface [mol/$m^3$]. |
| $c_{s,j,\text{max}}$ | Maximum electrode concentration [mol/$m^3$]. |
| $i_{0,j}$ | Exchange current density [A/$m^2$]. |
| $k_j$ | Reaction rate constant [$m^{2.5}$/s-$\text{mol}^{0.5}$]. |
| $l$ | Cartesian coordinate along the cell's thickness. |

Manuscript received July 27, 2017; revised November 10, 2017 and November 29, 2017; accepted December 23, 2017. Date of publication January 23, 2018; date of current version May 1, 2018. *(Corresponding author: Simona Onori.)*

The authors were with the Department of Automotive Engineering, Clemson University, Greenville, SC 29607 USA. They are now with the Department of Energy Resources Engineering, Stanford University, Stanford, CA 94305 USA (e-mail: aallam@stanford.edu; sonori@stanford.edu).

Color versions of one or more of the figures in this paper are available online at http://ieeexplore.ieee.org.

Digital Object Identifier 10.1109/TIE.2018.2793194

| | |
|---|---|
| $r$ | Radial coordinate. |
| $t$ | Temporal coordinate. |
| $t_0^+$ | Transference number. |
| $\epsilon_j$ | Active volume fraction of solid phase. |
| $\epsilon_{e,j}$ | Porosity. |
| $\kappa$ | Electrolyte conductivity [S/m]. |
| $\kappa^{\text{eff}}$ | Effective electrolyte conductivity [S/m]. |
| $\eta_j$ | Overpotential [V]. |
| $\theta_{j,100\%}$ | Reference stoichiometry ratio at 100% SOC. |
| $\theta_{j,0\%}$ | Reference stoichiometry ratio at 0% SOC. |
| Subscript $j$ | Refers to anode, separator, or cathode. |
| Subscript ol | Open loop. |

## I. Introduction

LITHIUM-ION battery technology has come to the forefront for the electrification of the automotive powertrain, owing to its superior power and energy density. To ensure longevity, safety, and reliable operation of lithium-ion batteries, a BMS is deployed in electrified vehicles [1]. Internal variables of a lithium-ion battery, such as the lithium concentration in the electrodes and internal temperature, can provide the BMS with information on the SOC and SOH of the battery. This information is translated by the BMS for the benefit of the driver, into driver-related terms like vehicle range capability and RUL of the electrified powertrain. Further, real-time knowledge of the SOC and SOH can be harnessed in accomplishing safety-critical tasks like the SOC and capacity-based cell balancing, thermal balancing, and health-conscious battery control. However, note that the internal states that provide information on the SOC and SOH of the battery are not directly available for measurement. This serves as a motivation to design an accurate real-time battery electrochemical state estimator that can be an essential component in an advanced BMS.

### A. Background and Related Work

The fundamental element in the design of an electrochemical state estimator is an accurate electrochemical model that describes the dynamics of a lithium-ion battery. Electrochemical-based battery models, derived from the porous electrode and the concentrated solution theory, via the volume-averaging [2] or homogenization theory [3], use the first-principles modeling approach to describe the transport of lithium ions in the solid and liquid phase through a system of nonlinear partial differential algebraic equations. These models provide physical insights into the battery by predicting the internal states, such as lithium concentration and overpotential [2], unlike the typically used lumped-parameter equivalent circuit battery models [4]. Despite the high accuracy of the electrochemical models, they are computationally expensive, rendering them unsuitable for real-time applications, thus laying out the motivation for the development of tractable reduced-order electrochemical models. The SPM is one such tractable model that is derived by approximating the electrode by a single spherical particle, assuming a uniform current density in each electrode, and neglecting the diffusion and migration dynamics of the lithium ions in the electrolyte [5]. The SPM offers low computational complexity and yet provides insight into the electrochemical dynamics of the battery, making it suitable for control-oriented applications with low C-rates (C-rate is defined as the rate of current in normalized form, $C-\text{rate} = I_{\text{batt}}/Q_{\text{nom}}$), typically seen in EVs. More recently, the SPM has been improved by including electrolyte dynamics to obtain an ESPM that can accurately predict the battery behavior at higher currents [6]–[8].

Various electrochemical model-based state estimation algorithms including Bayesian filters [9], [10], Luenberger observers [6], [11], SMO [12], nonlinear observers [13], and the more sophisticated PDE-based backstepping observer [8], [14] have been implemented. A common thread of discussion among electrochemical-based estimators is the issue of weak observability in estimating the lithium concentration in both electrodes from the cell's output voltage. The cell's output voltage is obtained as a difference of electrode potentials that are nonlinear functions of lithium concentration in the respective electrodes. Due to this peculiar structure, one can estimate the difference between electrode potentials, but not the individual electrode potential, and by extension the lithium concentration in individual electrodes, resulting in weak observability [9]. Three methods have been proposed to estimate lithium concentration in electrochemical-based estimator designs despite the existence of weak observability.

1) *Method 1:* The number of lithium moles in both electrodes is assumed to be conserved [8], [9], [12]–[14]. This establishes an algebraic relationship between lithium concentration in both electrodes, thereby resulting in an observable electrochemical model [9], wherein the concentration of only one electrode needs to be estimated.
2) *Method 2:* The lithium concentration in an individual electrode is estimated by assuming a perfect open-loop model of the other electrode [10].
3) *Method 3:* Adding a temperature sensor allows the relationship between the electrode's entropic heat and its lithium concentration to be exploited, thereby improving the observability of lithium concentration in both electrodes from the voltage and surface temperature measurements [15].

Note that Methods 1 and 2 estimate lithium concentration in one electrode, whereas Method 3 estimates the concentration in both electrodes. However, all three methods have drawbacks. In Method 1, the assumption of lithium conservation in both electrodes will not hold true in the event of aging. Degradation mechanisms like the SEI layer growth or lithium plating involve side reactions that consume cyclable lithium ions, invalidating the assumption of lithium conservation [15]. Evidently, an estimator designed under this assumption will not guarantee convergence as the cell ages. In Method 2, it is imperative that the open-loop model of the electrode be initialized correctly. In reality, the correct initial value of the concentration may not be known resulting in an incorrect initialization of the open-loop model and the subsequent divergence of the estimated concentration from its true value. On the other hand, although Method 3 overcomes the drawbacks of earlier methods, it relies on thermal measurements, which adds additional hardware cost in the form

of temperature sensors for each cell. Moreover, an analytical proof of convergence for the concentration estimation in both electrodes is lacking.

### B. Contributions and Paper Outline

The major contribution of this paper is the design of an electrochemical model-based observer that can estimate the lithium concentration in both cathode and anode, concurrently, by rejecting the assumption of lithium conservation, in the face of incorrect initializations, and in the absence of thermal measurements. Doing so gives the ability to track the bulk and surface concentration in both electrodes that provide information on the amount of usable capacity and output voltage or instantaneous power, respectively [10]. The combined information promises to offer more freedom to employ battery control algorithms with wider operational limits for both electrodes and minimize or monitor degradation mechanisms that occur at either electrode.

The remainder of this paper is organized as follows. In Section II, the governing equations describing the ESPM are laid out. Further, a constrained optimization problem is formulated for parameter identification and subsequent validation results are presented. Section III introduces the interconnected sliding mode observer structure for the simultaneous estimation of bulk and surface concentration in the cathode and anode and presents the derivation of a rigorous stability proof to substantiate the existence of a convergent interconnected observer. In Section IV, the effectiveness of the interconnected observer is illustrated under measurement noises and parametric uncertainties. This is followed by conclusions and directions for future research in Section V.

## II. Electrochemical Battery Model

The ESPM is a reduced-order electrochemical model that describes the lithium concentration dynamics in the solid and electrolyte phase, and also predicts the overpotential of the electrodes. Further, the mass transport and kinetic parameters of the ESPM, and the OCP of both electrodes are considered to be dependent on temperature. The model used in this study is simplified by assuming a single lumped resistance.

### A. Governing Equations

The transport of lithium in the solid phase of each electrode is described by the spherical diffusion equation given by the following PDE and its respective boundary conditions

$$\begin{cases} \dfrac{\partial c_{s,j}}{\partial t} = D_{s,j}\left[\dfrac{2}{r}\dfrac{\partial c_{s,j}}{\partial r} + \dfrac{\partial^2 c_{s,j}}{\partial r^2}\right] \\ \left.\dfrac{\partial c_{s,j}}{\partial r}\right|_{r=0} = 0; \quad \left.\dfrac{\partial c_{s,j}}{\partial r}\right|_{r=R_j} = \dfrac{\pm I_{\text{batt}}}{F \cdot a_{s,j} \cdot D_{s,j} \cdot A \cdot L_j}. \end{cases} \tag{1}$$

The diffusion dynamics of lithium ions in the electrolyte phase in the Cartesian coordinate ($l \in [0, L]$, where $L = L_n + L_s + L_p$) along the thickness of the cell is modeled through the following PDE and its respective boundary conditions

$$\begin{cases} \epsilon_{e,j}\dfrac{\partial c_e}{\partial t} = \dfrac{\partial}{\partial l}\left(D_e^{\text{eff}}\dfrac{\partial c_e}{\partial l}\right) + \left(1 - t_0^+\right)\dfrac{\pm I_{\text{batt}}}{F \cdot A \cdot L_j} \\ \left.\dfrac{\partial c_e}{\partial l}\right|_{l=0} = \left.\dfrac{\partial c_e}{\partial l}\right|_{l=L} = 0 \\ D_{e,n}^{\text{eff}}\left(\dfrac{\partial c_{e,n}}{\partial l}\right)\Big|_{l=L_n} = D_{e,s}^{\text{eff}}\left(\dfrac{\partial c_{e,s}}{\partial l}\right)\Big|_{l=L_n} \\ D_{e,s}^{\text{eff}}\left(\dfrac{\partial c_{e,s}}{\partial l}\right)\Big|_{l=L_n+L_s} = D_{e,p}^{\text{eff}}\left(\dfrac{\partial c_{e,s}}{\partial l}\right)\Big|_{l=L_n+L_s} \end{cases} \tag{2}$$

where $D_{e,j}^{\text{eff}} = D_e \epsilon_{e,j}^{1.5}$. The potential gradient in the electrolyte phase is given by

$$\kappa^{\text{eff}}\frac{\partial^2 \phi_e}{\partial x^2} + \frac{2R_g T \kappa^{\text{eff}}\left(1 - t_0^+\right)}{F}\frac{\partial^2 \ln c_e}{\partial x^2} + \frac{\pm I_{\text{batt}}}{A \cdot L_j} = 0 \tag{3}$$

where $\kappa_j^{\text{eff}} = \kappa \epsilon_{e,j}^{1.5}$. Integrating the aforementioned equation across the thickness of the cell, we obtain the potential difference in the electrolyte phase as [16]

$$\Delta\Phi_e = \frac{2R_g T\left(1 - t_0^+\right)}{F} \cdot \ln\frac{c_e(L)}{c_e(0)} - \frac{I_{\text{batt}}}{2 \cdot A}\left(\frac{L_n}{K_n^{\text{eff}}} + \frac{2 \cdot L_{\text{sep}}}{K_{\text{sep}}^{\text{eff}}} + \frac{L_p}{K_p^{\text{eff}}}\right). \tag{4}$$

The overpotential of each electrode is obtained from the Butler–Volmer kinetic equation that describes the rate of intercalation and deintercalation of lithium ions as

$$\eta_j = \frac{R_g T}{0.5F} \cdot \sinh^{-1}\left(\frac{I_{\text{batt}}}{2 \cdot a_{s,j} \cdot A \cdot L_j \cdot i_{0,j}}\right) \tag{5}$$

where $i_{0,j} = k \cdot \sqrt{c_{e,0} \cdot c_{s,j,\text{surf}} \cdot (c_{s,j,\max} - c_{s,j,\text{surf}})}$. And the nonlinear terminal voltage of the ESPM is

$$V = \left[U_p\left(c_{s,p,\text{surf}}\right) + \eta_p\left(c_{s,p,\text{surf}}, I_{\text{batt}}\right)\right] - \left[U_n\left(c_{s,n,\text{surf}}\right) + \eta_n\left(c_{s,n,\text{surf}}, I_{\text{batt}}\right)\right] + \Delta\Phi_e - I_{\text{batt}} \cdot R_l. \tag{6}$$

Henceforth, to make the notation simpler, the terms are represented as nonlinear functions ($h(\cdot)$) such that $[U_p(c_{s,p,\text{surf}}) + \eta_p(c_{s,p,\text{surf}}, I_{\text{batt}})] = h_1(c_{s,p,\text{surf}}, I_{\text{batt}})$, $[U_n(c_{s,n,\text{surf}}) + \eta_n(c_{s,n,\text{surf}}, I_{\text{batt}})] = h_2(c_{s,n,\text{surf}}, I_{\text{batt}})$, and $\Delta\Phi_e = -h_3(c_e, I_{\text{batt}})$, thereby reducing the nonlinear output voltage equation to $V = h_1(c_{s,p,\text{surf}}, I_{\text{batt}}) - h_2(c_{s,n,\text{surf}}, I_{\text{batt}}) - h_3(c_e, I_{\text{batt}}) - R_l u$.

Furthermore, the capacity of each electrode, $Q_j$, for a fresh cell, in terms of its geometrical parameters is given by [9]

$$Q_j = F \cdot A \cdot L_j \cdot \epsilon_j \cdot c_{s,j,\max} \cdot (\theta_{j,100\%} - \theta_{j,0\%})/3600. \tag{7}$$

In this paper, the solid-phase diffusion coefficient ($D_{s,j}$) and the reaction rate constant ($k_j$) have an Arrhenius dependence on temperature as follows:

$$\begin{cases} D_{s,j}(T) = D_{s,j,\text{ref}} \cdot \exp\left[\frac{-E_{a,D,j}}{R_g}\left(\frac{1}{T} - \frac{1}{T_{\text{ref}}}\right)\right] \\ k_j(T) = k_{j,\text{ref}} \cdot \exp\left[\frac{-E_{a,k,j}}{R_g}\left(\frac{1}{T} - \frac{1}{T_{\text{ref}}}\right)\right] \end{cases} \tag{8}$$

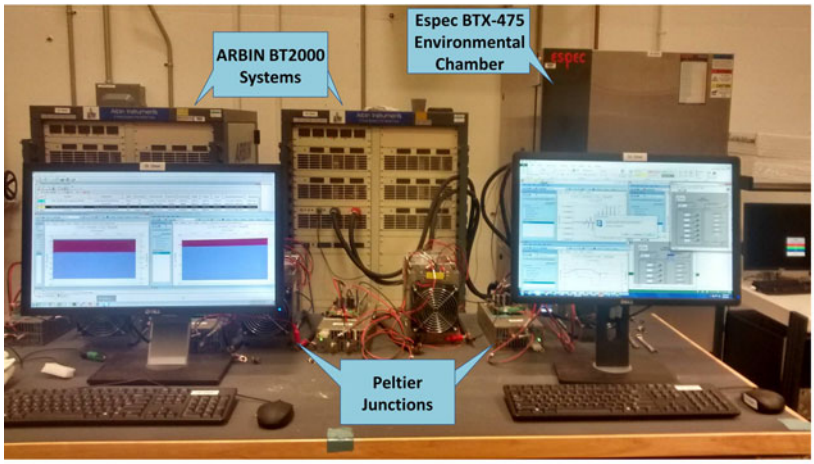


(a)

| Model | Sony VTC4 |
|---|---|
| Cathode Chemistry | NMC |
| Nominal Capacity | 2 Ah |
| Nominal Voltage | 3.6 V |
| Maximum Voltage | 4.2 V |
| Minimum Voltage | 2.5 V |

(b)

Fig. 1. Experimental setup for battery testing, at the Battery Aging and Characterization (BACh) Laboratory, Clemson University-International Center for Automotive Research (CU-ICAR), consists of two multichannel Arbin BT2000 battery testing equipments that apply standard or custom current profiles on the cell, five TE Technology's Peltier junctions and a ESPEC BTX-475 environmental chamber to maintain the surface temperature of the cells at the desired temperature set point, and (b) specifications of a cylindrical 18650, 2-Ah NMC Lithium-ion cell used in the experiments.

where $T_{\text{ref}} = 23\,^{\circ}\text{C}$ is the reference temperature. Also, the OCP $(U_j)$ of each electrode is dependent on the temperature $(T)$ given by Taylor's expansion as

$$U(c_{s,j,\text{surf}}, T) = U_j(c_{s,j,\text{surf}}, T_{\text{ref}}) + \frac{\partial U_j}{\partial T}(T - T_{\text{ref}}). \quad (9)$$

Note that the activation energy $E_{a,D,j}, E_{a,k,j}$ in (8), and $\partial U_j/\partial T$ in (9) are borrowed from [7]. Further, the electrolyte phase diffusion and conductivity are considered to depend on temperature through the empirical relationship described in [17], given as

$$\begin{cases} D_e(T) & = 10^{-\left[4.43 + \frac{54}{T-(229+c_{e,0})} + 0.22c_{e,0}\right]} \\ \kappa(T) & = c_{e,0}[(-10.5 + 0.074T - 6.96\times 10^{-5}T^2) \\ & \quad + c_{e,0}(0.668 - 0.0178T - 2.8\times 10^{-5}T^2) \\ & \quad + c_{e,0}^2(0.494 - 8.86\times 10^{-4}T)]^2. \end{cases}$$

For the implementation of the aforementioned described model, the solid phase spherical diffusion PDEs in (1) are radially discretized into $N+1$ concentration nodes, and the electrolyte phase PDEs in (2) are discretized in the Cartesian coordinate, along the thickness of the cell, into $M+1$ concentration nodes, using the FDM. The detailed discretization procedure can be found in [7] and [18]. The discretization results in a system of $2N+M$ ODEs. The system of ODEs and the nonlinear voltage equation is reformulated into a general state-space form as follows:

$$\begin{aligned} \dot{x}_1 &= A_{11}x_1 + B_1 u \\ \dot{x}_2 &= A_{22}x_2 + B_2 u \\ \dot{x}_3 &= A_{33}x_3 + B_3 u \\ y &= h_1(x_{1,N}, u) - h_2(x_{2,N}, u) - h_3(x_3, u) - R_l u \end{aligned} \quad (10)$$

where the state vector $x \in \mathbb{R}^{(2N+M)}$ is $x = [x_1, x_2, x_3]^T$, wherein $x_1$ and $x_2$ are the concentration state variables at the discretized $N$ nodes of the positive and negative spherical electrodes, respectively, given by $x_1 = [c_{s,p,1}, c_{s,p,2}, \ldots, c_{s,p,N}]^T$, $x_2 = [c_{s,n,1}, c_{s,n,2}, \ldots, c_{s,n,N}]^T$, and $x_3$ is the concentration state variables at the discretized $M$ nodes of the electrolyte phase, given by $x_3 = [c_{e,1}, c_{e,2}, \ldots, c_{e,M}]^T$. The input current $u = I_{\text{batt}}$ and output voltage $y = V$. Furthermore, square matrices $A_{11}, A_{22} \in \mathbb{R}^{N\times N}$ and $A_{33} \in \mathbb{R}^{M\times M}$, and column vectors $B_1, B_2 \in \mathbb{R}^{N\times 1}$ and $B_3 \in \mathbb{R}^{M\times 1}$ are the state and input matrices containing the electrochemical model parameters that need to be identified.

*Remark 1:* The state variables $x_1$ and $x_2$ hold the values of all the concentration nodes of the cathode and anode, respectively. Hence, knowing $x_1$ and $x_2$ will enable the computation of bulk and surface concentration of both electrodes. The bulk concentration is computed through volume averaging as [9], [13]

$$c_{s,j,\text{bulk}} = \frac{1}{\frac{4}{3}\pi N^3}\sum_{i=1}^{N} 4\pi i^2 c_{s,j,i} \quad (11)$$

and the surface concentration is the concentration at the last discretized node, which is $x_{1,N} = c_{s,p,N}$ and $x_{2,N} = c_{s,n,N}$ for the cathode and anode, respectively.

## B. ESPM Identification and Validation Results

Experiments are conducted on cylindrical lithium-ion cells to characterize the parameters of the ESPM using experimentally measured current and voltage data, and subsequently validate the same. The experimental procedure entails maintaining the cell at a constant desired temperature and subjecting it to a predetermined input current (drive cycle) and log the resulting output voltage. The experimental setup to carry out the battery testing experiments is shown in Fig. 1(a).

TABLE I
IDENTIFIED ESPM PARAMETERS

| Optimization Variable | Parameter | Value |
|---|---|---|
| $\lambda_1$ | $L_n$ [m] | $60.6 \times 10^{-6}$ |
| $\lambda_2$ | $L_p$ [m] | $52.5 \times 10^{-6}$ |
| $\lambda_3$ | $A$ [m$^2$] | 0.093 |
| $\lambda_4$ | $c_{s,n,\max}$ [mol m$^{-3}$] | 27920 |
| $\lambda_5$ | $c_{s,p,\max}$ [mol m$^{-3}$] | 45711 |
| $\lambda_6$ | $\epsilon_n$ [$-$] | 0.53 |
| $\lambda_7$ | $\epsilon_p$ [$-$] | 0.54 |
| $\lambda_8$ | $D_{s,n,\mathrm{ref}}$ [m$^2$ s$^{-1}$] | $1.74 \times 10^{-14}$ |
| $\lambda_9$ | $D_{s,p,\mathrm{ref}}$ [m$^2$ s$^{-1}$] | $2.98 \times 10^{-14}$ |
| $\lambda_{10}$ | $k_n$ [m$^{2.5}$ mol$^{-0.5}$ s$^{-1}$] | $3.16 \times 10^{-10}$ |
| $\lambda_{11}$ | $k_p$ [m$^{2.5}$ mol$^{-0.5}$ s$^{-1}$] | $5.96 \times 10^{-10}$ |
| $\lambda_{12}$ | $R_l$ [$\Omega$] | 0.026 |
| $\lambda_{13}$ | $L_s$ [m] | $21 \times 10^{-6}$ |
| $\lambda_{14}$ | $\epsilon_s$ [$-$] | 0.58 |

The ESPM parameter identification is devised as an optimization problem subject to geometrical and functional constraint on the lithium-ion battery under study, shown in Fig. 1(b). A set of 14 ESPM parameters that need to be identified are denoted by vector $\lambda$, $\lambda = [\lambda_1, \lambda_2, \ldots, \lambda_{14}]$. A constraint is placed on the cathode capacity, as the limiting electrode ($Q_{\mathrm{nom}} = Q_p$), to ensure that the identified values are physically relevant. The ESPM in (11) is implemented in MATLAB using the in-built ode23s solver. The parameters are initialized with approximate guesses from the literature. The objective of the optimization routine is to minimize the RMS error between the ESPM predicted output voltage and the experimentally measured cell voltage, by trying to satisfy the constraint on capacity. The constrained optimization problem for parameter identification is summarized as follows:

$$\underset{\lambda_{\min}<\lambda<\lambda_{\max}}{\operatorname{argmin}} \quad \sqrt{\frac{1}{M}\sum_{k=1}^{M}\left(V_{\mathrm{expt},k} - y_k(\lambda)\right)^2}$$

subject to:

$$\begin{aligned}
\dot{x}_{1,k} &= A_{11}(\lambda)\, x_{1,k} + B_1(\lambda)\, u_k \\
\dot{x}_{2,k} &= A_{22}(\lambda)\, x_{2,k} + B_2(\lambda)\, u_k \\
\dot{x}_{3,k} &= A_{33}(\lambda)\, x_{3,k} + B_3(\lambda)\, u_k \\
y_k &= h_1(x_{1,N,k}, u_k, \lambda) - h_2(x_{2,N,k}, u_k, \lambda) \\
&\quad - h_3(x_{3,k}, u_k, \lambda) - \lambda_{12} u_k \\
Q_{\mathrm{nom}} &= \frac{F \cdot \lambda_3 \cdot \lambda_7 \cdot \left(\theta_{p,100\%} - \theta_{p,0\%}\right) \cdot \lambda_5}{3600}
\end{aligned}$$

where $V_{\mathrm{expt},k}$ and $u_k$ are the cell voltage and input current that are experimentally measured, and $M$ is the total number of measured voltage or current samples at a sampling frequency of 1 Hz.

The constrained optimization problem for the identification of ESPM parameters is solved using a global optimization algorithm (Genetic Algorithm) over the experimentally collected voltage and current data for a HPPC test [19] at 23 °C. Table I reports the parameters with their identified values. Note that the value for $R_j$ is borrowed from [6]. The HPPC current profile, the evolution of SOC (calculated from Coulomb counting), and the comparison of the ESPM predicted voltage against the measured voltage are plotted in Fig. 2. The RMS voltage error obtained from the identification is 8.7 mV, which shows that the ESPM performs well at predicting the real battery response.

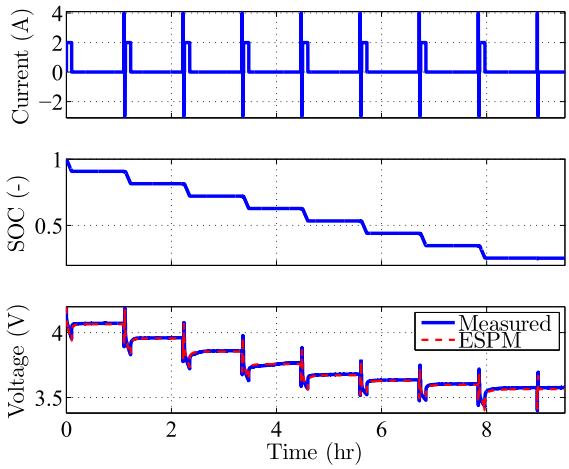


Fig. 2. Input current profile, SOC profile, and the voltage comparison obtained from identification tests between experimental data and ESPM output over the HPPC test at 23 °C.

Since the ESPM parameters have been identified on the HPPC profile with lower C-rate at room temperature (23 °C), we validate the model against 1) a custom staircase profile to verify the model's accuracy for higher current values, and 2) a UDDS (x2) profile to verify the model's accuracy at a different temperature. The custom staircase profile uses high discharge and charge pulses, ranging from $\pm 2$ to 6 C-rate. The current profile is applied to a cell with initial SOC of 55%, placed inside a Peltier Junction with its temperature set to 23 °C. The UDDS cycle is a charge depleting profile derived for an EV and scaled to a single cell [8]. The UDDS (x2) profile is applied to a cell with initial SOC of 100%, placed inside a Peltier Junction with its temperature set to 45 °C. The measured current is supplied to the identified ESPM and the resulting simulated voltage is compared with the measured cell voltage. The current profiles, the evolution of SOC, and the comparison of ESPM predicted voltage with the measured voltage for the custom staircase and UDDS (x2) profiles are plotted in Figs. 3 and 4, respectively. The RMS voltage error with respect to the experimentally measure voltage is 13.5 and 12.3 mV for the staircase and UDDS drive cycles, respectively. This shows that the identified ESPM reasonably replicates the battery behavior at higher C-rates and different temperatures.

*Remark 2:* The SPM can be derived from the aforemenioned validated ESPM by assuming uniform concentration and potential gradient in the electrolyte phase, effectively, neglecting the equations given in (2) and (3), respectively. The derived SPM, is a lower order model suitable for the observer design, due to its low computational demands. Also, this enables a systematic comparison of the SPM-based observer's performance against the fully validated ESPM, which is a more complicated and higher order model compared to the SPM. The state-space

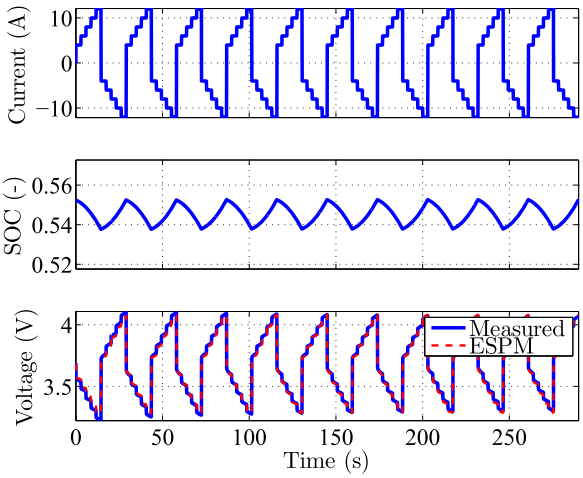


Fig. 3. Input current profile, SOC profile, and the voltage comparison obtained from the validation test between experimental data and ESPM output over a high C-rate staircase pulse profile at 23 °C.

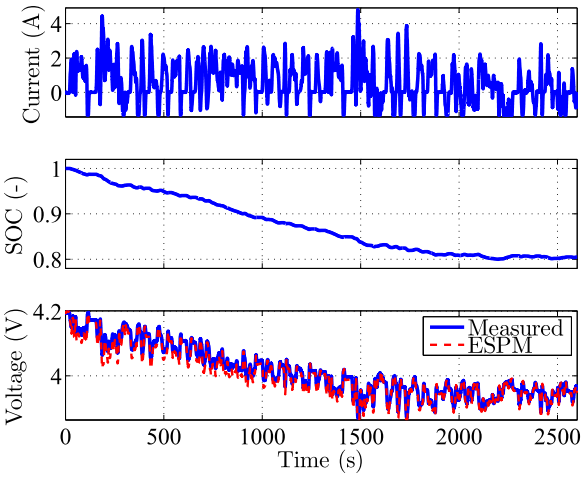


Fig. 4. Input current profile, SOC profile, and the voltage comparison obtained from validation tests between experimental data and ESPM output over the UDDS (x2) profile at 45 °C.

formulation for the SPM, after neglecting the electrolyte concentration and potential dynamics, is as follows:

$$\begin{aligned}\dot{x}_1 &= A_{11}x_1 + B_1 u \\ \dot{x}_2 &= A_{22}x_2 + B_2 u \\ y &= h_1\left(x_{1,N}, u\right) - h_2\left(x_{2,N}, u\right) - R_l u. \end{aligned} \tag{12}$$

## III. Interconnected Observer Design

The SPM in (12) is observable only if the knowledge of the input current and output voltage are sufficient to reconstruct the concentration state variables of the cathode and anode. Study in [9] shows that both the electrode concentration states in the SPM are not guaranteed to be observable from the output voltage. Moreover, in [10], without relying on the assumption of lithium conservation, it is shown that the concentration state variables of a single electrode (cathode or anode) are observable if the state variables of the other electrode are known through open-loop model simulation, also described in Method 2 of Section I-A. This has led to the implementation of the single electrode concentration observer structure, used for SOC estimation in [10] and shown in Fig. 5(a). The single electrode observer in Fig. 5(a) estimates cathode concentration state variables while simulating the anode model in open loop. Alternatively, the anode states could be estimated by simulating the cathode in open loop. The open-loop model provides the pseudomeasurements required to estimate the output voltage. The error between the measured and estimated voltage, along with the measured current, act as the inputs to the single electrode observer Fig. 5(a).

In this structure, the open-loop anode model is assumed to be initialized correctly to provide perfect pseudomeasurements. Note that in the event of incorrect initialization due to lack of knowledge of the initial conditions, the open-loop anode model response will be erroneous. It is understood that if the open-loop model response is incorrect, the output voltage computed from the pseudomeasurements will be wrong, resulting in the cathode concentration state estimate to diverge from the true value. However, if there exists a way to correct the open-loop anode model, then the estimated cathode states would converge to the true values. To achieve that, we propose to 1) introduce a similarly structured observer for the anode, in parallel, to estimate the anode states and simulate the cathode in open loop, and 2) interconnect the estimated states of the cathode and anode observers, such that the cathode concentration state estimate is fed to the cathode open-loop model in the anode observer, and the anode concentration state estimate is fed to the anode open-loop model in the cathode observer. The proposed interconnected observer structure is shown in Fig. 5(b).

It is worth mentioning that implementing two single electrode observers in parallel will not guarantee convergence if the open-loop models are incorrectly initialized. Rather, the presence of the bidirectional interconnection, between the two observers, updates the incorrect open-loop model with the estimated states, progressively correcting the open-loop model response, and thereby, driving the estimated values of the closed-loop model to converge to the correct values. The proposed observer is different from the single electrode observer in [10] in the following ways:

1) The proposed observer can concurrently estimate the states of both electrodes unlike the single electrode observer;
2) The estimates converge, despite an incorrectly initialized open-loop model;
3) An analytical proof for the convergence of the concentration state estimates can be derived.

### A. Sliding Mode Observer

For the interconnected structure, the sliding mode observer [20] is preferred due to its ability to provide robust estimates in the presence of modeling uncertainties and measurement noises. Recent studies have used the SMO for battery state estimation [12], [21], [22]. While [12] and [21] use a constant gain, [22] uses an adaptive switching gain to suppress chattering during

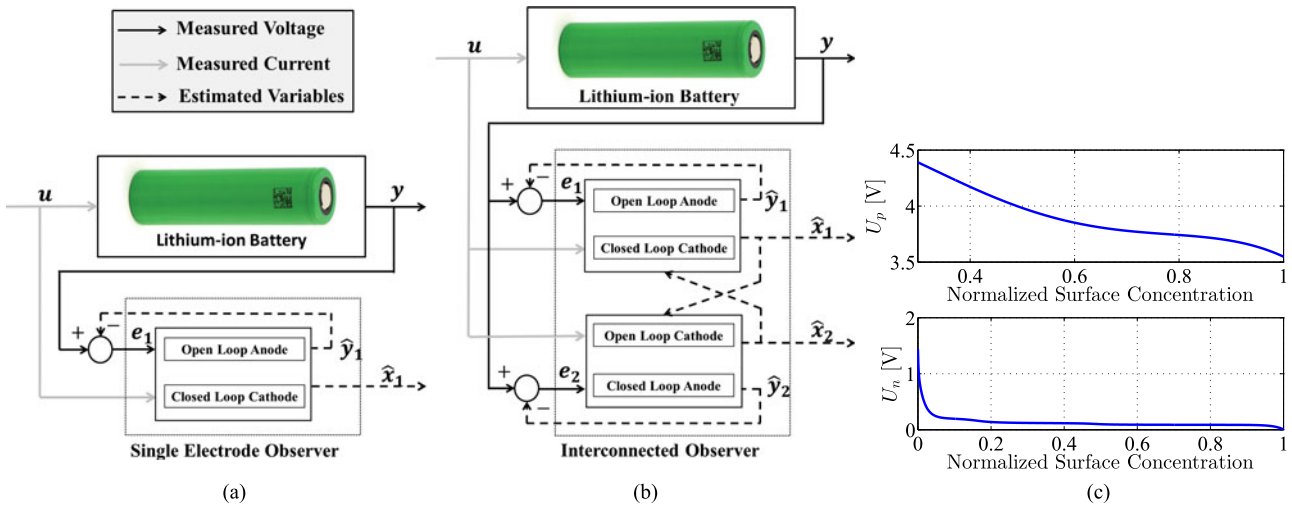


Fig. 5. (a) Single electrode concentration observer from [10], (b) proposed interconnected observer structure for concurrent estimation of concentration in both electrodes, and (c) experimentally measured OCP curves for NMC and Graphite at 25 °C [6].

estimation. The SMO equations in this study are similar in design to [21], however, note that the SMO in [21] is based on a linearized equivalent circuit battery model, whereas the SMO proposed here is for a novel interconnected structure based on an electrochemical model with nonlinearity in the output equation. The observer for each electrode includes a linear output injection term and a discontinuous output injection term. Taking the interconnection between the two observers into consideration, the structure for the cathode and anode observers for the SPM in (12) is formulated as

$$\begin{cases} \dot{\hat{x}}_1 &= A_{11}\hat{x}_1 + B_1 u + G_1\left(y-\hat{y}_1\right) + G_{v1}\,\mathrm{sgn}\left(y-\hat{y}_1\right) \\ \dot{\hat{x}}_{2,\mathrm{ol}} &= A_{22}\hat{x}_2 + B_2 u \\ \hat{y}_1 &= h_1\left(\hat{x}_{1,N}, u\right) - h_2\left(\hat{x}_{2,N,\mathrm{ol}}, u\right) - R_l u \end{cases} \tag{13}$$

and

$$\begin{cases} \dot{\hat{x}}_{1,\mathrm{ol}} &= A_{11}\hat{x}_1 + B_1 u \\ \dot{\hat{x}}_2 &= A_{22}\hat{x}_2 + B_2 u + G_2\left(y-\hat{y}_2\right) + G_{v2}\,\mathrm{sgn}\left(y-\hat{y}_2\right) \\ \hat{y}_2 &= h_1\left(\hat{x}_{1,N,\mathrm{ol}}, u\right) - h_2\left(\hat{x}_{2,N}, u\right) - R_l u \end{cases} \tag{14}$$

where $G_1, G_2, G_{v1}$, and $G_{v2} \in \mathbb{R}^N$ are constant observer gains, the subscript ol stands for open-loop model state variables, and the discontinuous injection term is defined as

$$\mathrm{sgn}\left(y-\hat{y}_1\right) = \begin{cases} 1, & \text{if } y-\hat{y}_1 > 1 \\ -1, & \text{if } y-\hat{y}_1 < 1 \end{cases}$$

$$\mathrm{sgn}\left(y-\hat{y}_2\right) = \begin{cases} 1, & \text{if } y-\hat{y}_2 > 1 \\ -1, & \text{if } y-\hat{y}_2 < 1. \end{cases}$$

The error, $e$, is defined as the difference between the true value and the estimated value, such that $e_1 = x_1 - \hat{x}_1$ and $e_2 = x_2 - \hat{x}_2$. From (13), the error dynamics for the two observers is written as

$$\begin{cases} \dot{e}_1 &= A_{11}e_1 - G_1\left(y-\hat{y}_1\right) - G_{v1}\,\mathrm{sgn}\left(y-\hat{y}_1\right) \\ \dot{e}_2 &= A_{22}e_2 - G_2\left(y-\hat{y}_2\right) - G_{v2}\,\mathrm{sgn}\left(y-\hat{y}_2\right). \end{cases} \tag{15}$$

Further, the output error of the cathode and anode observer is defined as: $y-\hat{y}_1 = [h_1(x_{1,N},u) - h_1(\hat{x}_{1,N},u)] - [h_2(x_{2,N},u) - h_2(\hat{x}_{2,N,\mathrm{ol}},u)] = \tilde{h}_1(e_{1,N}) - \tilde{h}_2(e_{2,N,\mathrm{ol}})$, and similarly, $y-\hat{y}_2 = \tilde{h}_1(e_{1,N,\mathrm{ol}}) - \tilde{h}_2(e_{2,N})$.

*Remark 3:* The error in the surface concentration of both electrodes, $e_{1,N}$ and $e_{2,N}$, is related to the state error vectors $e_1$ and $e_2$ through an output distribution matrix $C \in \mathbb{R}^{1\times N}$, where $C = [0,0,\ldots,0,1]$, as $e_{1,N} = Ce_1$ and $e_{2,N} = Ce_2$.

*Remark 4:* As the lithium concentration in the cathode increases, the concentration in the anode decreases, and vice versa. Thus, during estimation, the following condition will always hold true: $\mathrm{sgn}(e_1) = -\mathrm{sgn}(e_2)$, and hence, it also follows that $\mathrm{sgn}(\tilde{h}_1(e_{1,N})) = -\mathrm{sgn}(\tilde{h}_2(e_{2,N}))$.

*Remark 5:* We can write

$$\begin{aligned} \mathrm{sgn}\left(y-\hat{y}_1\right) &= \mathrm{sgn}\left(\tilde{h}_1\left(e_{1,N}\right) - \tilde{h}_2\left(e_{2,N,\mathrm{ol}}\right)\right) \\ &= -\mathrm{sgn}\left(\tilde{h}_2\left(e_{2,N,\mathrm{ol}}\right) - \tilde{h}_1\left(e_{1,N}\right)\right). \end{aligned} \tag{16}$$

And since $\mathrm{sgn}(h_2(e_{2,N,\mathrm{ol}})) = -\mathrm{sgn}(h_1(e_{1,N}))$ is deduced from Remark 4, it is understood that $\mathrm{sgn}(\tilde{h}_2(e_{2,N,\mathrm{ol}}) - \tilde{h}_1(e_{1,N}))$ will always be equal to sign of the first term in the difference equation inside the sign function, that is: $\mathrm{sgn}(\tilde{h}_2(e_{2,N,\mathrm{ol}}))$. Thus, the following properties will hold true:

$$\begin{aligned} \mathrm{sgn}\left(y-\hat{y}_1\right) &= -\mathrm{sgn}\left(\tilde{h}_2\left(e_{2,N,\mathrm{ol}}\right)\right) \\ \text{and likewise,}\quad \mathrm{sgn}\left(y-\hat{y}_2\right) &= \mathrm{sgn}\left(\tilde{h}_1\left(e_{1,N,\mathrm{ol}}\right)\right). \end{aligned} \tag{17}$$

*Proposition 1:* The nonlinear output functions $h_1$ and $h_2$ are strictly monotonously decreasing functions in $x_{1,N}$ and $x_{2,N}$, respectively, and bounded, as seen in Fig. 5(c). The gradient of

the nonlinear functions can be written as [8]

$$-\gamma_{p,\min} \leq \frac{\partial h_1}{\partial x_{1,N}} \leq -\gamma_{p,\max}$$

$$\text{and} \quad -\gamma_{n,\min} \leq \frac{\partial h_2}{\partial x_{2,N}} \leq -\gamma_{n,\max} \tag{18}$$

where $\gamma_{p,\min}, \gamma_{p,\max}, \gamma_{n,\min}, \gamma_{n,\max} \in \mathbb{R}_{>0}$, and $\mathbb{R}_{>0}$ is set of strictly positive real numbers. The aforementioned slope can be interpreted as the change in $h_1$ and $h_2$ due to the estimation error in $x_{1,N}$ and $x_{2,N}$, that is: $e_{1,N}$, $e_{1,N,\text{ol}}$ and $e_{2,N}$, $e_{2,N,\text{ol}}$. From Remark 3, with respect to the maximum bound, we can write $\tilde{h}_1(e_{1,N}) \leq -\gamma_{p,\max} C e_1$ and $\tilde{h}_2(e_{2,N}) \leq -\gamma_{n,\max} C e_2$.

Next, the asymptotic stability of the error dynamics is investigated using Lyapunov's stability analysis.

*Theorem 1:* If the choice of gains $G_1$, $G_2$, $G_{v,1}$, and $G_{v,2}$ satisfies the following inequalities, $G_1 < 0$, $G_2 > 0$, $G_{v1} < -G_1|\gamma_{n,\max} C e_{2,\text{ol}}|$, and $G_{v2} > -G_2|\gamma_{p,\max} C e_{1,\text{ol}}|$, then the estimation error dynamics of the interconnected sliding mode observer described in (14) and (15) are asymptotically stable.

*Proof.* Let $V_O$ be the candidate Lyapunov function for the interconnected observers given by

$$V_O = \frac{1}{2} e_1^T e_1 + \frac{1}{2} e_2^T e_2. \tag{19}$$

Taking derivative of $V_O$ with respect to time

$$\begin{aligned}\dot{V}_O &= e_1^T \dot{e}_1 + e_2^T \dot{e}_2 \\ &= e_1^T \left(A_{11} e_1 - G_1 \left(y - \hat{y}_1\right) - G_{v1} \operatorname{sgn}\left(y - \hat{y}_1\right)\right) \\ &\quad + e_2^T \left(A_{22} e_2 - G_2 \left(y - \hat{y}_2\right) - G_{v2} \operatorname{sgn}\left(y - \hat{y}_2\right)\right).\end{aligned}$$

From Proposition 1

$$\begin{aligned}\dot{V}_O \leq\ & e_1^T \left(A_{11} + G_1 \gamma_{p,\max} C\right) e_1 + e_2^T \left(A_{22} - G_2 \gamma_{n,\max} C\right) e_2 \\ & + e_1^T \left(G_1 \tilde{h}_2\left(e_{2,N,\text{ol}}\right) - G_{v1} \operatorname{sgn}\left(y - \hat{y}_1\right)\right) \\ & - e_2^T \left(G_2 \tilde{h}_1\left(e_{1,N,\text{ol}}\right) + G_{v2} \operatorname{sgn}\left(y - \hat{y}_2\right)\right).\end{aligned}$$

Using Remark 3, Proposition 1, and the property of sign function, yields

$$\operatorname{sgn}\left(\tilde{h}_1\left(e_{1,N,\text{ol}}\right)\right) = \frac{\tilde{h}_1\left(e_{1,N,\text{ol}}\right)}{|\tilde{h}_1\left(e_{1,N,\text{ol}}\right)|} \leq -\frac{\gamma_{p,\max} C e_{1,\text{ol}}}{|\gamma_{p,\max} C e_{1,\text{ol}}|}$$

$$\operatorname{sgn}\left(\tilde{h}_2\left(e_{2,N,\text{ol}}\right)\right) = \frac{\tilde{h}_2\left(e_{2,N,\text{ol}}\right)}{|\tilde{h}_2\left(e_{2,N,\text{ol}}\right)|} \leq -\frac{\gamma_{n,\max} C e_{2,\text{ol}}}{|\gamma_{n,\max} C e_{2,\text{ol}}|}.$$

Note that $|\gamma_{p,\max}|$ and $|\gamma_{n,\max}|$ are chosen as the maximum gradient of the cathode and anode OCP curves, given in Fig. 5(c). This ensures that the gains $G_{v,1}$ and $G_{v2}$ are selected by taking into account the maximum uncertainty that can be induced due to the open-loop model error. Finally, using Remark 5, we have

$$\begin{aligned}\dot{V}_O \leq\ & e_1^T \left(A_{11} + G_1 \gamma_{p,\max} C\right) e_1 + e_2^T \left(A_{22} - G_2 \gamma_{n,\max} C\right) e_2 \\ & - e_1^T \left(G_1 + \frac{G_{v1}}{|\gamma_{n,\max} C e_{2,\text{ol}}|}\right) \gamma_{n,\max} C e_{2,\text{ol}} \\ & + e_2^T \left(G_2 + \frac{G_{v2}}{|\gamma_{p,\max} C e_{1,\text{ol}}|}\right) \gamma_{p,\max} C e_{1,\text{ol}}.\end{aligned}$$

By choosing the gains $G_1$ to be small enough and $G_2$ to be large enough, such that the inequalities $G_1 < 0$ and $G_2 > 0$ are satisfied, the eigenvalues of $(A_{11} + G_1 \gamma_{p,\max} C)$ and $(A_{22} - G_2 \gamma_{n,\max} C)$ can be placed in the left half plane. This ensures that the first two terms in the aforementioned equation are negative definite. Next, from Remark 4, it is understood that $\operatorname{sgn}(e_1^T) = -\operatorname{sgn}(e_{2,\text{ol}})$, and $\operatorname{sgn}(e_2^T) = -\operatorname{sgn}(e_{1,\text{ol}})$. For $\dot{V}_O$ to be negative definite, the gains $G_{v1}$ and $G_{v2}$ must satisfy the inequalities $G_{v1} < -G_1|\gamma_{n,\max} C e_{2,\text{ol}}|$ and $G_{v2} > -G_2|\gamma_{p,\max} C e_{1,\text{ol}}|$. Therefore, $\dot{V}_O \leq 0$ and the error dynamics of the interconnected observer are asymptotically stable, which indicates that the concentration estimates of both electrodes will converge to their respective real values. ■

## IV. Implementation Results

The effectiveness of the proposed interconnected observer is validated against experimental data collected from the setup described in Section II-B. Typically, only current and voltage measurements are available. *In situ* measurement of bulk and surface concentration are not reasonable to acquire during battery operation. Owing to that, the estimated bulk and surface concentration of both electrodes by the SPM-based interconnected observer are compared with the higher order ESPM, which is fully validated in Section II-B. The normalized percentage error is used as the metric to quantify the estimation performance of bulk and surface concentration as

$$\begin{cases} e_{s,j,\text{bulk}} = \dfrac{\left(c_{s,j,\text{bulk}} - \hat{c}_{s,j,\text{bulk}}\right) \cdot 100}{\left(\theta_{j,100\%} - \theta_{j,0\%}\right) \cdot c_{s,j,\max}} \\ e_{s,j,\text{surf}} = \dfrac{\left(c_{s,j,\text{surf}} - \hat{c}_{s,j,\text{surf}}\right) \cdot 100}{\left(\theta_{j,100\%} - \theta_{j,0\%}\right) \cdot c_{s,j,\max}} \end{cases}$$

where $c_{s,j,\text{bulk}}$ and $c_{s,j,\text{surf}}$ are the bulk and surface concentration values from the ESPM, whereas $\hat{c}_{s,j,\text{bulk}}$ and $\hat{c}_{s,j,\text{surf}}$ are the bulk and surface concentration estimates from the SPM-based observer.

### A. Comparison With the Single Electrode Observer

A comparative study between the performance of the proposed interconnected observer and the single electrode observer [10], shown in Fig. 5(a), is carried out to appreciate the presence of bidirectional interconnections. The single electrode observer structure is implemented for the cathode and anode, separately, for this study. The experimental data are collected over the UDDS (x2) profile at 23 °C. Unlike [10], the observer states (including the open-loop model) are initialized with an error of 45%. The contrasting performance between both observer schemes is shown in Fig. 6. Evidently, the estimates from the single electrode observer structure never converge because the incorrect open-loop models have no way to correct themselves. On the other hand, the interconnected observer tracks the true values, and after the initial transient, the normalized percentage error for the bulk and surface concentration of both, cathode and anode, settles within 1.5% and 2.45% of their respective true values.

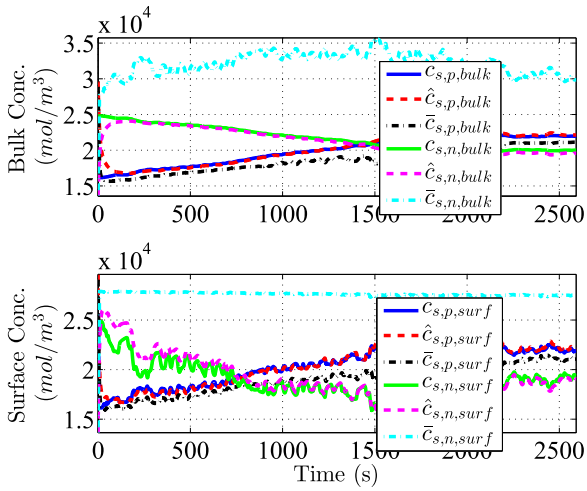


Fig. 6. Comparison of bulk and surface concentration estimation performance over the UDDS (x2) drive cycle between the proposed interconnected observer and the single electrode observer, with the ESPM $(c_{s,j,\text{bulk}}, c_{s,j,\text{surf}})$ as the truth model. The estimates of the interconnected observer are denoted by $\hat{c}_{s,j,\text{bulk}}$ and $\hat{c}_{s,j,\text{surf}}$ and that of the single electrode observer are $\bar{c}_{s,j,\text{bulk}}$ and $\bar{c}_{s,j,\text{surf}}$. An initial error of 45% is introduced in the observer states.

## B. Performance Over the Charge-Sustaining Drive Cycle

Notice that the OCP curves for both electrodes are relatively flat around the middle region, as seen in Fig. 5(c). This results in the concentration states having low sensitivity to the output during estimation. As a result, in this region, error in the open-loop model of the observers will be amplified in the state estimates. The performance of the interconnected observer is studied in the mid-SOC region of 55%, over the US06 (x4) drive cycle. The US06 current profile is derived from a charge-sustaining hybrid electric vehicle simulator and scaled to a single cell. To the best of our knowledge, concentration estimation results at mid-SOC regions have not been reported thoroughly in the literature. All the concentration states of the observer (including the open-loop model states) are initialized with an error of 45%. Despite the low sensitivity, the observer gives a good performance, as shown in Fig. 7, because the open-loop model is corrected at every time step, thereby driving the concentration estimates to converge to the true value. The normalized percentage error for the bulk and surface concentration of the cathode and anode is bounded within 1.28% and 2.64% of their respective true values. Further, the tracking can be improved by selecting proper observer gains $G_1$ and $G_2$. If $G_1$ and $G_2$ are large in magnitude, a small error will cause large oscillations in the estimated values, and if $G_1$ and $G_2$ are small in magnitude, then the estimate would remain unaffected and never reach the true value. Hence, the gains need to be tuned carefully such that the estimates can track the true value in finite time.

## C. Performance Under Measurement Noise and Parametric Uncertainty

Next, we evaluate the performance of the observer in the presence of measurement noise. During real-time operation, it

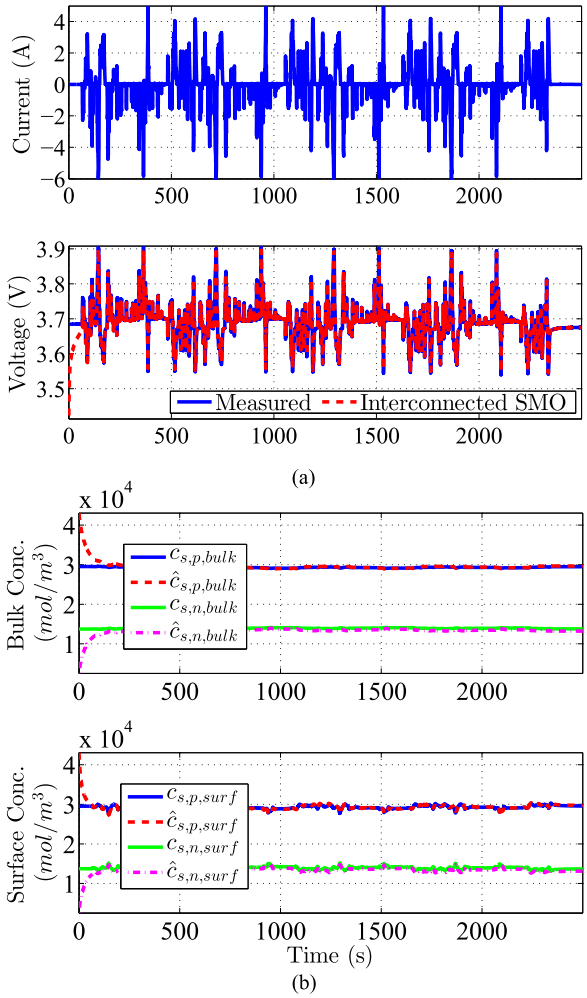


Fig. 7. Performance evaluation of the interconnected observer in the region of low output sensitivity. (a) Input current profile of the UDDS (x4) cycle and the voltage estimation comparison with the measured data. (b) Bulk concentration and surface concentration estimation validation against the ESPM. The initial SOC of the cell is 55%. The observer states are initialized with 45% error.

is possible that the measured signals may be corrupted due to sensor noise, and hence, it is important to test the proposed observer scheme in such conditions. In this section, the measured current and voltage signals, which are input to the interconnected observer, are corrupted with a zero-mean Gaussian noise with a standard deviation of 100 mA and 25 mV, respectively. The concentration states of the observer (including the open-loop model states) are initialized with an error of 45%. The interconnected observer's performance is shown in Fig. 8. The bulk and surface concentration estimation for the cathode and anode is confined to 1.65% and 2.18%, respectively. This shows that the interconnected observer provides robust estimates in the presence of external disturbances.

Further, it is important to assess the observer's effectiveness in the presence of uncertainties in model parameters that can be induced due to modeling errors during the identification process. Uncertainty is injected into the observer's model parameters by perturbing them around their identified values,

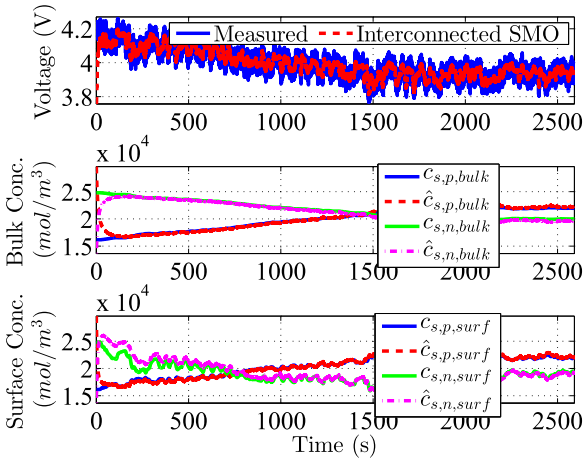


Fig. 8. Voltage, bulk concentration, and surface concentration estimation under measurement noises, at 23 °C, over the UDDS (x2) drive cycle. The current and voltage data are corrupted with zero mean Gaussian noise with standard deviation of 100 mA and 25 mV. The observer states are initialized with 45% error.

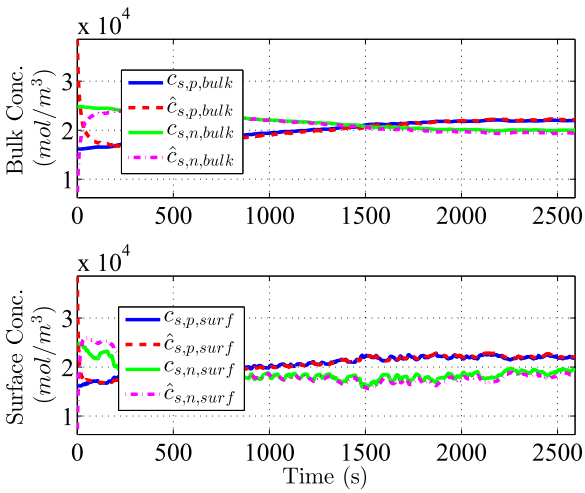


Fig. 9. Bulk and surface concentration estimation over the UDDS (x2) drive cycle with ESPM as the truth model at 23 °C under parametric uncertainties with $\hat{D}_{s,n,\mathrm{ref}} = 0.75 \cdot D_{s,n,\mathrm{ref}}$, $\hat{D}_{s,p,\mathrm{ref}} = 0.75 \cdot D_{s,p,\mathrm{ref}}$, and $\hat{R}_l = 1.25 \cdot R_l$. The observer states are initialized with 45% error.

such that $\hat{D}_{s,n,\mathrm{ref}} = 0.75 \cdot D_{s,n,\mathrm{ref}}$, $\hat{D}_{s,p,\mathrm{ref}} = 0.75 \cdot D_{s,p,\mathrm{ref}}$, and $\hat{R}_l = 1.25 \cdot R_l$, and the performance of the interconnected observer is studied. The bulk and surface concentration estimation plots are shown in Fig. 9. Clearly, the anode observer's estimates suffer due to the uncertainty in the parameters. Still, the normalized percentage error for the bulk and surface concentration estimation for both, cathode and anode, after the initial transient, never exceeds 1.5% and 4.6%, respectively.

## V. Conclusion

This paper presented a novel interconnected observer structure that can concurrently estimate the bulk and surface concentration of lithium in the cathode and anode. The ESPM is identified and experimentally validated for a cylindrical 18650, 2-Ah NMC Lithium-ion cell. The SPM, derived from the ESPM, is used for synthesis of the interconnected observer. The proposed observer does not assume conservation of lithium ions in both electrodes or require hardware for surface temperature acquisition. In addition, the convergence of the proposed observer is proved using Lyapunov's stability theory. Moreover, the performance of the observer is studied against experimental data and a higher order battery model (ESPM). Simulation results suggest that the interconnected observer provides robust estimates in the presence of parameter uncertainties and measurement noises. Future research will focus on developing an aging model for the synthesis of an SOH observer, in combination with the already proposed interconnected observer, to estimate the health of the anode or cathode, due to degradation mechanisms like the SEI layer growth and predict the RUL of the battery.

## References

[1] H. Rahimi-Eichi, U. Ojha, F. Baronti, and M.-Y. Chow, "Battery management system: An overview of its application in the smart grid and electric vehicles," *IEEE Ind. Electron. Mag.*, vol. 7, no. 2, pp. 4–16, Jun. 2013.

[2] M. Doyle, T. F. Fuller, and J. Newman, "Modeling of galvanostatic charge and discharge of the lithium/polymer/insertion cell," *J. Electrochem. Soc.*, vol. 140, no. 6, pp. 1526–1533, 1993.

[3] H. Arunachalam, S. Onori, and I. Battiato, "On veracity of macroscopic lithium-ion battery models," *J. Electrochem. Soc.*, vol. 162, no. 10, pp. A1940–A1951, 2015.

[4] S. Nejad, D. Gladwin, and D. Stone, "A systematic review of lumped-parameter equivalent circuit models for real-time estimation of lithium-ion battery states," *J. Power Sources*, vol. 316, pp. 183–196, 2016.

[5] S. Santhanagopalan, Q. Guo, P. Ramadass, and R. E. White, "Review of models for predicting the cycling performance of lithium ion batteries," *J. Power Sources*, vol. 156, no. 2, pp. 620–628, 2006.

[6] T. R. Tanim, C. D. Rahn, and C.-Y. Wang, "State of charge estimation of a lithium ion cell based on a temperature dependent and electrolyte enhanced single particle model," *Energy*, vol. 80, pp. 731–739, 2015.

[7] G. Fan, K. Pan, M. Canova, J. Marcicki, and X. G. Yang, "Modeling of li-ion cells for fast simulation of high c-rate and low temperature operations," *J. Electrochem. Soc.*, vol. 163, no. 5, pp. A666–A676, 2016.

[8] S. J. Moura, F. B. Argomedo, R. Klein, A. Mirtabatabaei, and M. Krstic, "Battery state estimation for a single particle model with electrolyte dynamics," *IEEE Trans. Control Syst. Technol.*, vol. 25, no. 2, pp. 453–468, Mar. 2017.

[9] D. Di Domenico, A. Stefanopoulou, and G. Fiengo, "Lithium-ion battery state of charge and critical surface charge estimation using an electrochemical model-based extended Kalman filter," *J. Dyn. Syst., Meas. Control*, vol. 132, no. 6, p. 061302-1–061302-11, 2010.

[10] A. Bartlett, J. Marcicki, S. Onori, G. Rizzoni, X. G. Yang, and T. Miller, "Electrochemical model-based state of charge and capacity estimation for a composite electrode lithium-ion battery," *IEEE Trans. Control Syst. Technol.*, vol. 24, no. 2, pp. 384–399, Mar. 2016.

[11] R. Klein, N. A. Chaturvedi, J. Christensen, J. Ahmed, R. Findeisen, and A. Kojic, "Electrochemical model based observer design for a lithium-ion battery," *IEEE Trans. Control Syst. Technol.*, vol. 21, no. 2, pp. 289–301, Mar. 2013.

[12] S. Dey, B. Ayalew, and P. Pisu, "Combined estimation of state-of-charge and state-of-health of Li-ion battery cells using SMO on electrochemical model," in *Proc. 13th Int. Workshop Variable Structure Syst.*, 2014, pp. 1–6.

[13] S. Dey, B. Ayalew, and P. Pisu, "Nonlinear robust observers for state-of-charge estimation of lithium-ion cells based on a reduced electrochemical model," *IEEE Trans. Control Syst. Technol.*, vol. 23, no. 5, pp. 1935–1942, Sep. 2015.

[14] S. J. Moura, N. A. Chaturvedi, and M. Krstić, "Adaptive partial differential equation observer for battery state-of-charge/state-of-health estimation via an electrochemical model," *J. Dyn. Syst., Meas. Control*, vol. 136, no. 1, pp. 011015-1–011015-11, 2014.

[15] S. Dey and B. Ayalew, "Real-time estimation of lithium-ion concentration in both electrodes of a lithium-ion battery cell utilizing electrochemical–thermal coupling," *J. Dyn. Syst., Meas. Control*, vol. 139, no. 3, pp. 031007-1–031007-10, 2017.
[16] E. Prada, D. Di Domenico, Y. Creff, J. Bernard, V. Sauvant-Moynot, and F. Huet, "Simplified electrochemical and thermal model of LiFePO4-graphite Li-ion batteries for fast charge applications," *J. Electrochem. Soc.*, vol. 159, no. 9, pp. A1508–A1519, 2012.
[17] L. O. Valøen and J. N. Reimers, "Transport properties of LiPF6-based li-ion battery electrolytes," *J. Electrochem. Soc.*, vol. 152, no. 5, pp. A882–A891, 2005.
[18] R. Ahmed, M. El Sayed, I. Arasaratnam, J. Tjong, and S. Habibi, "Reduced-order electrochemical model parameters identification and SOC estimation for healthy and aged li-ion batteries Part I: Parameterization model development for healthy batteries," *IEEE Trans. Emerg. Sel. Topics Power Electron.*, vol. 2, no. 3, pp. 659–677, Sep. 2014.
[19] *Battery Test Manual for Plug-In Hybrid Electric Vehicles*, United States DOE Vehicle Technologies Program, Dec. 2010, Revision 2.
[20] S. Drakunov, and V. Utkin, "Sliding mode observers. Tutorial," in *Proc. IEEE 34th Conf. Decision Control*, 1995, vol. 4, pp. 3376–3378.
[21] I.-S. Kim, "The novel state of charge estimation method for lithium battery using sliding mode observer," *J. Power Sources*, vol. 163, no. 1, pp. 584–590, 2006.
[22] X. Chen, W. Shen, Z. Cao, and A. Kapoor, "A novel approach for state of charge estimation based on adaptive switching gain sliding mode observer in electric vehicles," *J. Power Sources*, vol. 246, pp. 667–678, 2014.

**Anirudh Allam** (S'17) received the B.E. degree in electronics and telecommunication engineering from the University of Pune, Pune, India and the M.S. degree in automotive engineering from Clemson University, Clemson, SC, USA, in 2010 and 2015, respectively. He is currently working toward the Ph.D. degree with the Department of Energy Resources Engineering, Stanford University, Stanford, CA, USA.

His research interests include estimation, control, and degradation modeling of electrochemical energy storage systems.

**Simona Onori** (SM'15) received the Laurea degree (summa cum laude) in computer science engineering from the University of Rome "Tor Vergata," Rome, Italy, in 2003, the M.S. degree in electrical and computer engineering from the University of New Mexico, Albuquerque, NM, USA, in 2004, and the Ph.D. degree in control engineering from the University of Rome "Tor Vergata," in 2007.

She has been an Assistant Professor with the Energy Resources Engineering Department, Stanford University, Stanford, CA, USA, since October 2017. Formerly, she was an Assistant Professor with Clemson University-International Center for Automotive Research (CU-ICAR), since 2013, where she also held a joint appointment with the Electrical and Computer Engineering. She also holds visiting professor positions with the University of Trento, Trento, Italy, in 2014, the Beijing Institute of Technology, Beijing, China, in 2015, and the University of Orleans, Orléans, France, in 2016, and she is the PSG Distinguished Visiting Professor awarded by the Managing Trustee of the PSG College of Technology, Coimbatore, India, in 2017.

Dr. Onori was the recipient of the 2017 NSF CAREER award, the 2017 Clemson University College of Engineering and Science Dean's Faculty Fellows Award, the 2017 Clemson University Esin Gulari Leadership and Service Award, the 2016 Energy Leadership Award in the category Emerging Leader (for the Carolinas), the 2015 Innovision Award (South Carolina), the 2012 Lumley Interdisciplinary Research, and the 2011 Outstanding Technology Team Award, TechColumbus.